Lab on a Chip

Accepted Manuscript

This is an *Accepted Manuscript*, which has been through the Royal Society of Chemistry peer review process and has been accepted for publication.

Accepted Manuscripts are published online shortly after acceptance, before technical editing, formatting and proof reading. Using this free service, authors can make their results available to the community, in citable form, before we publish the edited article. We will replace this *Accepted Manuscript* with the edited and formatted *Advance Article* as soon as it is available.

You can find more information about *Accepted Manuscripts* in the **Information for Authors**.

Please note that technical editing may introduce minor changes to the text and/or graphics, which may alter content. The journal's standard **Terms & Conditions** and the **Ethical guidelines** still apply. In no event shall the Royal Society of Chemistry be held responsible for any errors or omissions in this *Accepted Manuscript* or any consequences arising from the use of any information it contains.

Lab on a Chip

Tunable self-imaging effect using hybrid optofluidic waveguides

Y. Shi,[a] L. Liang,[a] X. Q. Zhu,[a] X. M. Zhang[b] and Y. Yang*[a]

Multimode interference (MMI) is a typical self-imaging phenomenon and has been widely exploited for optical devices like couplers and splitters. Usually it utilizes solid waveguides only and thus has very limited tunabilities in the self-imaging properties. This paper reports our original work of tunable MMI using a hybrid optofluidic waveguide. It is generated by the diffusion between miscible flows in a microchannel and consists of two parts: gradient-index liquid-liquid waveguide for light modulation and step-index liquid-solid waveguide for image-forming. Simulation and experiments have shown successful realizations of the real-time tuning of self-imaging properties. For detail, the image point (focal spot) width could be modulated from 7 μm to 16 μm, and the self-imaging period changes in the range of 500 μm by varying the fluid properties. It is foreseeable that such a hybrid optofluidic waveguide may find wider applications in lab-on-a-chip systems and optical devices.

Introduction

Self-imaging effect is an interference effect that was first observed by Talbot[1] in 1836 and then explained by Lord Rayleigh[2] half a century later. In free space, it features the periodic reproduction of the grating pattern at regular distances when a transmission grating is irradiated by a monochromatic plane wave. The realization of such effect using slab waveguides was proposed by Bryngdahl[3] and elaborated by Ulrich[4]. Usually, the slab waveguide has a single-mode section connected with a multimode section. The single-mode section provides a confined light source (close to a point light source), which propagates in the multimode section by total internal reflection and generates the self-imaging patterns by the multimode interference (MMI). Unlike other optical phenomena for tight focusing such as superlenses,[5,6] the MMI-based self-imaging effect has unique properties such as simple design, polarization independence, low loss, and small size, making it attractive for many applications such as beam splitters,[7,8] multiplexers,[9] Mach-Zehnder interferometric switches,[10] phase shifters,[11] decoder switches,[12] gas sensors[13] and couplers[14]. In addition to the slab waveguides, some advanced waveguide designs have also been reported. One way is to change the original MMI structure for the modulation of self-imaging pattern, but at the cost of complicated process and high precision machining.[15-18] Besides, once fabricated, the waveguides have very limited tunabilities in shape and refractive index (RI) due to the use of solid materials. Graded-index waveguides by ion-exchange have also the same problems.[19,20] A variable structure by
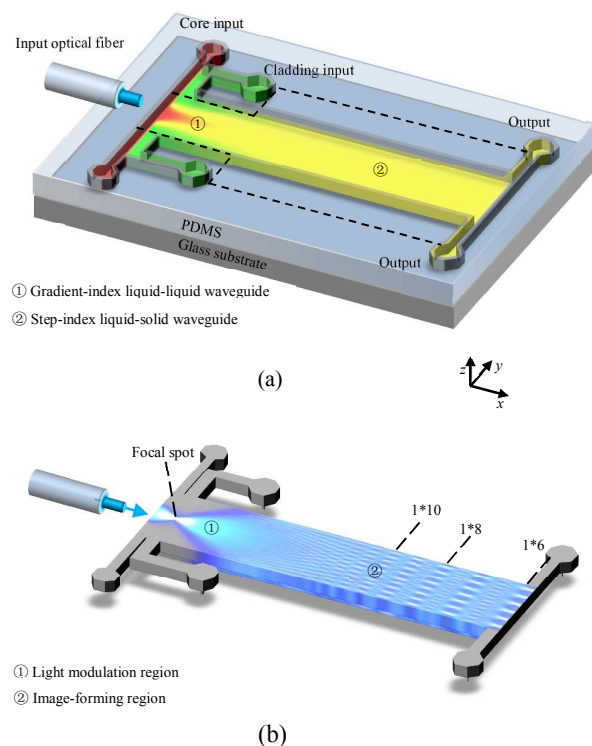
mechanical force[21] can solve this problem, but its instability and inaccuracy become a great obstacle to its application.

In contrast, liquid media can be reconfigured and replaced easily, allowing much larger tunability in RI and shape than solid media. This has inspired the creation of optofluidic technology that combines the optics and the microfluidics for liquid-based devices and systems.[22] It has applications in many fields[23-31], optofluidic waveguide structure[26-31] is one of the typical application, such as step-index[29,30] or gradient-index[28,31] ones. However, to realize the MMI-based self-imaging effect, two combined waveguides are needed. Generally, the Reynolds number indicates the tendency of a flow to develop turbulence. For the flows in microfluidic devices, they have mostly a low Reynolds number and are often laminar,[32] enabling the creation of stable graded index by the diffusion across the interface of miscible liquids[31]. This is one of the unique and beneficial features of the optofluidics. Moreover, liquid properties such as flow rates, concentration and shape could be adjusted easily, and even the fluid materials can be replaced.

In this paper, we will demonstrate the tunable self-imaging effect using a hybrid optofluidic waveguide. Unlike the solid counterparts that consist of fixed structures (a single-mode waveguide connected with a multimode waveguide), the hybrid optofluidic waveguide is generated simply by injecting three miscible flows in a rectangle microchannel. In the front of the microchannel, the diffusion between the miscible flow streams produces a graded-index liquid-liquid waveguide to converge light, and realize the modulation of imaging patterns. In the latter, complete diffusion makes the RI distribution in the microchannel uniform, light can be total internally reflected at the liquid-solid interface. A step-index liquid-solid waveguide for MMI is obtained after the front region. The hybrid optofluidic waveguides will show more flexibility as compared to the traditional solid counterparts by controlling the flow rates and liquid materials. It may find a variety

[a.] School of Physics & technology, Wuhan University, Wuhan 430072, China. E-mail: yangyiys@whu.edu.cn
[b.] Department of Applied Physics, Hong Kong Polytechnic University, Hung Hom, Kowloon, Hong Kong

Please do not adjust margins
Lab on a Chip
Page 2 of 5

① Gradient-index liquid-liquid waveguide

② Step-index liquid-solid waveguide

(a)

① Light modulation region

② Image-forming region

(b)

Fig. 1 Self-imaging effect by the MMI in the hybrid optofluidic waveguide. (a) The concentration distribution and the resulted self-imaging pattern (b) formed by three miscible flows in the hybrid optofluidic chip.

of applications in tunable lab-on-a-chip optical devices, such as couplers, splitters, switches and sensors.

Working principle and conceptual design

The working principle of our hybrid optofluidic waveguide is shown in Fig. 1. It has a short region with the gradient index (GRIN) distribution, following by a long section of uniform medium. When collimated light propagates through the GRIN region, it is converged to a focal spot as the outer rays tend to bend inwards,[31] similar to the focusing effect in GRIN lenses or GRIN fibers[33-35]. This focused light serves as a confined light source for the liquid-solid waveguide to produce the self-imaging pattern by the MMI (see Fig. 1b), as does in the solid MMI waveguides.[3,4] The device design is illustrated in Fig. 1a. It consists of three miscible flows pumped into a microchannel from four separate inlets. The central flow stream has a relative higher RI n_{core} and acts as the core of liquid-liquid waveguide, and the two side flow streams have a relative lower RI n_{clad} and function as the cladding layers. Necessarily, both n_{core} and n_{clad} are higher than n_p, which is the RI of poly-dimethyl siloxane (PDMS), a material for microchannel. This ensures the self-imaging effect in the latter.

A GRIN profile is formed in the modulation region due to the mutual diffusion[31] as shown in Fig. 1a. Then the concentration difference gradually diminishes along the microchannel, until a uniform mixing is obtained after a certain distance. This distance is short for slow flows and small concentration difference. With these,

the short GRIN region focuses the input light and the long uniformly-mixed region enables the MMI.

Convection and diffusion proceed when different flow streams from each inlet meet up in the channel. The convection-diffusion equation is[36]

$$\partial c / \partial t = D \nabla^2 c - u \nabla c \tag{1}$$

where c, D, u and t denote the concentration, the diffusion coefficient, the flow velocity and the time, respectively. When a stable concentration distribution is reached, it has $\partial c / \partial t = 0$. The concentration distribution for the steady-state flow in the microchannel in 2D has also been studied.[37] Here we choose an x-y coordinate system and let the flow direction be along x, the channel width along y. The difference of initial RI Δn is actually very small, i.e. $\Delta n / n \ll 1$. Especially, there is a quadratic index in each cross-section in the area of core flow.[31] Consequently, light rays bend moderately toward the central line when they propagate approximately along the x-axis, and then all of them converge to near a single focal spot as the phases of the different rays are almost the same at the focal spot, resulting in the well-known self-focusing effect. Actually, we can take the mixed liquid after the focal spot as a uniform multimode waveguide, so that the electric field profile is written as:[38]

$$E(y, L_{MMI}) = \varepsilon(y) \exp(-jk n_{eff} L_{MMI} + j\pi / 4) \tag{2}$$

here $\varepsilon(y)$ is the symmetrical electric field of input waveguide, k the wavenumber, n_{eff} the effective RI. And L_{MMI} is the period of the MMI as given by $L_{MMI} = (n_{eff} w^2)/\lambda$, w the width of microchannel, λ the wavelength of incident light and n_{eff} the average RI of mixed liquid as expressed by

$$n_{eff} = \frac{v_{core} w_{core} n_{core} + 2 v_{clad} w_{clad} n_{clad}}{v_{core} w_{core} + 2 v_{clad} w_{clad}} = \frac{v_{core} n_{core} \eta + v_{clad} n_{clad}(1-\eta)}{v_{core} \eta + v_{clad}(1-\eta)} \tag{3}$$

where v_{core} and v_{clad} denote the velocity of core flow and cladding flow, w_{core} and w_{clad} are the width of core flow and cladding flow, respectively. $\eta = w_{core} / w$ represents the proportion of space occupied by the core flow. It can be seen from equation (2) and (3) that the variation of any of v_{core}, n_{core}, v_{clad} or n_{clad} would cause the change of n_{eff}, which in turn alters L_{MMI}. In other words, the period of MMI can be tuned by varying the properties of flows.

Experimental results and discussions

In the first place, we have simulated the RI distribution in the microchannel. The methods are elaborated below and the results are shown in Fig. 2a. Unless otherwise specified, we choose the channel width $w = 100$ μm, the core width $w_{core} = 40$ μm, $n_{core} = 1.432$, $n_{clad} = 1.410$, $n_p = 1.405$, the flow velocities $v_{core} = v_{clad} = 500$ μm/s and the wavelength $\lambda = 532$ nm. They are also the parameters for experimental study. As shown in Fig. 2a, a small dome-shaped region of RI distribution is formed, the length in the longitudinal direction is shorter than 600 μm. After that, the RI distribution becomes almost uniform. For further details, the RI in the lateral direction at $x = 50$ μm is plotted in Fig. 2c. Within the core flow region, it is close to the quadratic relation, which is one of the ideal distributions for the focusing GRIN lenses[31]. The RI along the
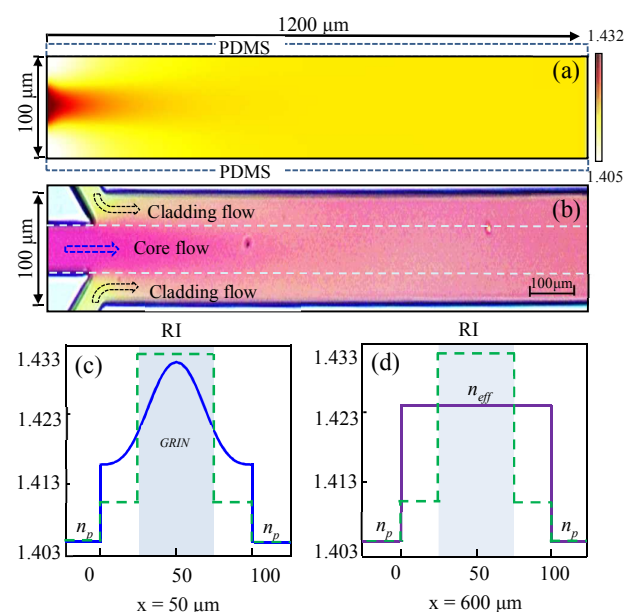
Fig. 2 Stable RI distribution in the main channel by simulation (a) and the experimental result (b). Step-index profile (green line) become smooth because of diffusion. (c) Lateral RI distribution at $x = 50$ μm (blue line), which is close to the quadratic distribution in the core flow region (the shadowed region). (d) Longitudinal RI distribution becomes uniform along the microchannel, which becomes stable at $x \geq 600$ μm.

central line of the microchannel drops rapidly and becomes flat after $x = 600$ μm as shown in Fig. 2d, indicating almost uniform RI, which is required for the MMI as discussed above.

The waveguide structure is fabricated by using the standard soft lithography process[28,29]. Firstly, a 100 μm layer of SU8 photoresist (Micro-Chem, SU8-50) is spin-coated onto a silicon wafer. After

pre-baking, the master is exposed to UV light under a glass/chromium mask using a mask aligner (OAI, 506). This treated master generates a positive bas-relief of photoresist on the surface and can be used as a mold for PDMS (Dow corning, Sylgard 184). PDMS prepolymer is then poured over the master and stored in an oven for 1h at 75℃. The PDMS replica is then peeled form the master and sealed against a flat PDMS slab to form the microchannels after plasma oxidation. Different liquids are injected into the microchannel from each inlet as the core or cladding of waveguide. A single-mode optical fiber is aligned to the centre of core flow and is then fixed on the substrate by UV epoxy. A PDMS lens is employed to collimate the light from the fiber end. The core inlet and the cladding inlet are 40 μm and 30 μm wide, respectively; the main microchannel is 2 cm long and 100 μm high.

And then, we conduct an experiment to study the diffusion in the same microchannel. For direct visualization, the core flow contains the red dye and the cladding flows have the yellow dye. When the flows are slow ($v_{core} = v_{clad} = 500$ μm/s), the diffusion patterns are shown in Fig. 2b. It can be seen that dyes start to diffuse at the near end of the main channel and mix with each other quickly. This matches the simulated pattern in Fig. 2a. For fast flows, it needs a much longer distance for complete diffusion. This would cause slow GRIN changes in both the lateral and longitudinal directions and would affect the focal length and the self-imaging pattern.

To verify the effectiveness of the conceptual design, we have simulated the light propagation in the microchannel as shown in Fig. 3a. A clear focal spot is seen right after the dome-like region and then a self-imaging pattern is formed in the uniform region. After that, optical experiments are conducted using the same chip. The results are shown in Fig. 3b-3g. The material of the central flow stream for experiment is ethylene glycol ($n_{core} = 1.432$), while the material of cladding is the mixture of de-ionized water and ethylene
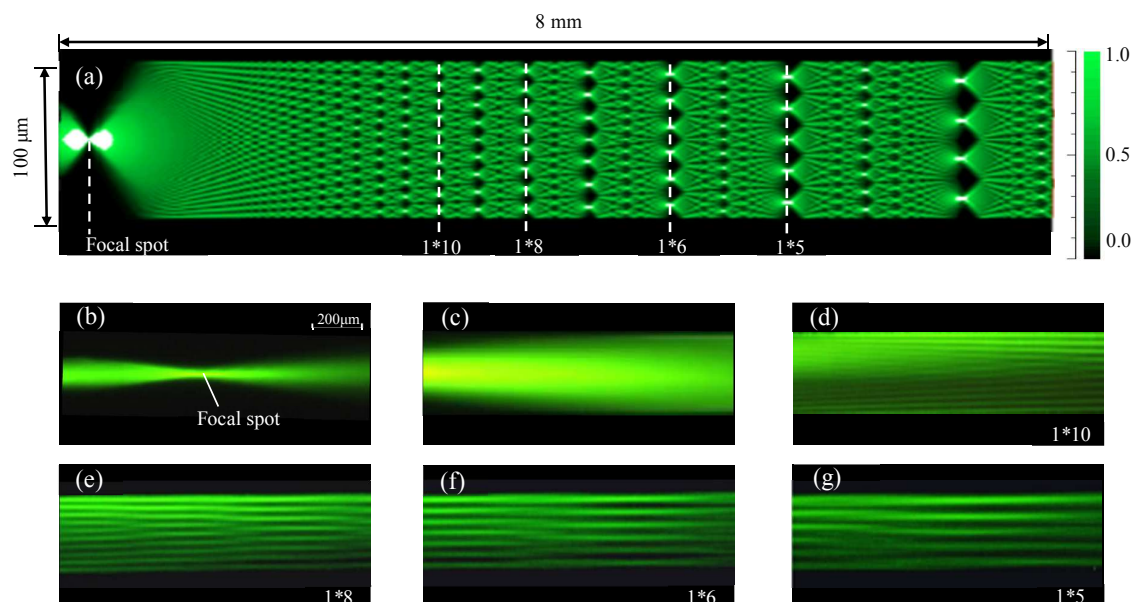
Fig. 3 Properties of self-imaging. The self-imaging interference pattern (a) in the microchannel illuminated by green light λ = 532 nm in simulation results. (b-g) Photos of the imaging patterns along the longitudinal direction of microchannel. The images are observed on the same chip in dye experiment and the width of each lens is 1250 μm. Not to scale.
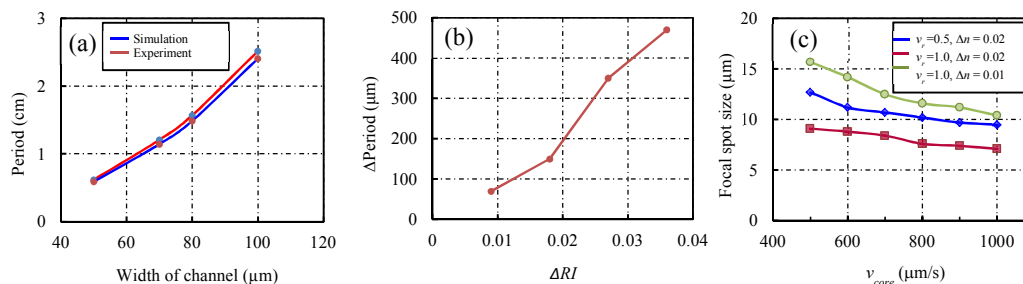
Fig. 4 (a) The period of MMI changes with the width of channel while the width of core keeps 30 μm all the time. (b) Liquid materials with different RI could be used to affect the period, and n_{clad} = 1.410, $\Delta RI = n_{core} - n_{clad}$, $v_{core} = v_{clad}$ = 500 μm/s. (c) The size of focal spot could be modulated by flow velocity and RI. $v_r = v_{clad}/v_{core}$, $\Delta n = n_{core} - n_{clad}$, and n_{core} = 1.432 all the time.

glycol (80 % $(CH_2OH)_2$ and 20 % DI water in mass, measured in experiment) with n_{clad} = 1.410. The flow velocities of the core and the cladding are kept the same at 500 μm/s. The selection of these two materials is intended to reduce the influence of the liquid interfaces among different flow streams. Meanwhile, the RI of PDMS is 1.405, smaller than either n_{core} or n_{clad}. Therefore, the condition of total internal reflection for the MMI is satisfied in both the width and thickness directions. The wavelength of parallel light is 532 nm (green), illuminated by a single-mode optical fiber with NA = 0.12, and the intensity profile of incident light follows the Gaussian distribution. Fig. 3b shows the focusing of light by the GRIN region. Meanwhile, Fig. 3c-3g show the real interference patterns (sub-images) at different positions along the longitudinal direction. Fig. 3c is the region right after the focal spot, where the light starts to diverge. Further away, bright fringes appear but the number of fringe goes down gradually from 10 to 5 (see Fig. 3d-3g),

Fig. 5 Tuning of the self-imaging patterns. The simulated results when (a) $v_{clad} = v_{core}$ = 600 μm/s and (b) $v_{clad} = v_{core}$ = 400 μm/s; the experimental results when (c) $v_{clad} = v_{core}$ = 600 μm/s and (d) $v_{clad} = v_{core}$ = 400 μm/s. In all cases, there are n_{core} = 1.432 and n_{clad} = 1.410.

and even smaller after longer propagation distance.

Discussion

The self-imaging period follows the approximatively same law for the solid and the liquid MMI. Fig. 4a plot the change of self-imaging period with the channel width, given by the simulation and experiments. Obviously, the results of experiments closely approximate those of simulation.

When the two cladding flows are consistent, changing flow velocities or the width of each flow can adjust the position of focal spot and make a relatively small change of the self-imaging period due to $\Delta n/n \ll 1$. Different materials can be replaced for a wide range of adjustments as shown in Fig. 4b. The size of focal spot is changed to adjust the sizes of sub-images and the whole interference pattern in the same way. For example, the size of focal spot is 10.2 μm when $v_{core} = v_{clad}$ = 1000 μm/s, but it becomes 16.0 μm when $v_{core} = v_{clad}$ = 500 μm/s. The relationship between the focal spot size and the flow properties is plotted in Fig. 4c. The diffraction at the port as a disturbance in the solid MMI[38] is solved in the optofluidic waveguides due to the presence of a GRIN profile.

The flow velocity slightly influences the self-imaging patterns based on the assumption that the fluidic concentration after the focal spot is homogeneous. But the RI distribution is actually not completely uniform behind the focal spot. Medium can be divided into two regions according to the role of imaging along the microchannel: modulation region and image-forming region. Each part has its own function: the image-forming region is a basic part for the formation of MMI, while the modulation region affects the regularity of the images.

The optical path difference is given by $\Delta = \int n(s)ds$ if the RI of materials $n(s)$ varies along the path s. In the area that is not too far away from the focal spot, the RI decreases from the centre to both sides as the two liquids are not completely diffused. Therefore, an inverted parabolic wavefront of sub-images is formed as the rays on both sides need a longer distance s to achieve the same optical path, in comparison to the rays near the central line as shown in Fig. 5a and 5b, which are simulation results of different flow velocity. And different distributions of optical intensity can be seen as well. This kind of effects caused by the inhomogeneity of liquid near the focal spot is proved by the corresponding experimental results in Fig. 5c and 5d, and becomes weaker along the spreading distance because of the diffusion. On the contrary, it shows a straight line in the solid
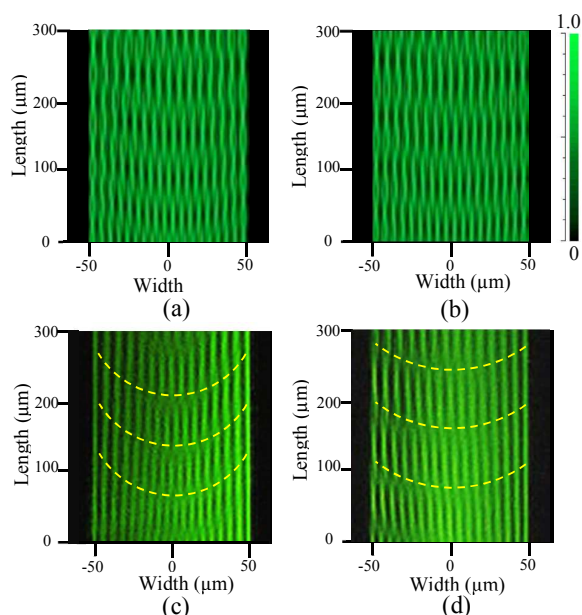
MMI devices at longitudinal cross-section. The properties of three flow streams can be adjusted to tune the self-imaging patterns in real time. As a matter of fact, the off-axial focal spot can be formed if the two claddings have different flow velocities, and the self-imaging effect with the different period can also occur at the same time.[39]

Conclusions

In conclusion, we demonstrates tunable self-imaging function using a hybrid optofluidic waveguide. Different from the traditional solid counterparts, the hybrid optofluidic waveguide consists of two regions: (1) A liquid-liquid diffused waveguide in front for light tuning, (2) A liquid-solid waveguide latter for pattern generation. Results have shown successful realizations of the real-time tuning of self-imaging properties. For detail, the image point width realizes adjustment from 7 μm to 16 μm, and a tunable period of the self-imaging is achieved up to 500 μm by varying the fluid properties. A unique inverted parabolic wavefront of sub-images is also implemented and modulated. It shows that such a hybrid optofluidic waveguide may find wider applications in lab-on-a-chip systems and optical devices.

Acknowledgement

Notes and references

1. H. F. Talbot, *Philos. Mag.*, 1836, **9**, 401-407.
2. Lord Rayleigh, *Philos. Mag.*, 1881, **11**, 196-205.
3. O. Bryngdahl, *J. Opt. Soc. Amer.*, 1973, **63**, 416-419.
4. R. Ulrich, *Nouv. Rev. Opt.*, 1975, **6**, 253-262.
5. X. Zhang and Z. W. Liu, *Nat. Mater.*, 2008, **7**, 435-441.
6. G. Yuan, E. T. F. Rogers, T. Roy, G. Adamo, Z. Shen, and N. I. Zheludev, *Sci. Rep.*, 2014, **4**, 6333.
7. M. Blahut and A. Opilski, *Opto-Electron. Rev.*, 2001, **9**, 293-300.
8. J. M. Heaton, R. M. Jenkins, D. R. Wight, J. T. Parker, J. C. H. Birbeck and K. P. Hilton, *Appl. Phys. Lett.*, 1992, **61**, 1754-1756.
9. K. C. Lin and W. Y. Lee, *Electron. Lett.,* 1996, **32**, 1259-1261.
10. R. Dangel and W. Lukosz, *Opt. Commun.*, 1998, **156**, 63-76.
11. R. M. Lorenzo, J. I. Bailon, P. Fernandez, J. C. Aguado, I. de Miguel, E. J. Abril, and M. Lopez, *Opt. Commun.*, 1997, **174**, 435-443.
12. Z. W. Chen, Z. J. Li, B. J. Li, *Opt. Express*, 2006, **14**, 2671-2678.
13. T. Mazingue, R. K. Kribich, P. Etienne, Y. Moreau, *Opt. Commun.*, 2007, **278**, 312-316.
14. J. Leuthold, J. Eckner, E. Gamper, P. A. Besse, and H. Melchior, *J. Lightwave Technol.*, 1998, **16**, 1228-1239.
15. Q. Z. Deng, L. Liu, X. B. Li and Z. P. Zhou, *Opt. Lett.*, 2014, **39**, 5590-5593.
16. Y. C. Shi, D. X. Dai, S. L. He, *Opt. Commun.*, 2005, **253**, 276-282.
17. M. Bachmann, P. A. Besse, H. Melchior, *Appl. Opt.*, 1995, **34**, 6898-6910.
18. J. S. Li, H. Liu, L. Zhang, *Appl. Opt.*, 2014, **53**, 5024-5028.
19. S. Das, D. Geraghty, S. Honkanen and N. Peyghambarian, *Proc. SPIE*, 2000, **3936**, 239-247.
20. M. Blahut and D. Kasprzak, *Acta Physica Polonica A*, 2009, **116**, 257–260.
21. Q. Lai, M. Bachman, W. Hunziker, P. A. Besse, and H. Melchior, *Electron. Lett.*, 1996, **32**, 1576-1577.
22. D. Psaltis, S. R. Quake and C. H. Yang, *Nature*, 2006, **442**, 381-386.
23. C. Monat, P. Domachuk and B. J. Eggleton, *Nat. Photonics*, 2007, **1**, 106-114.
24. V. R. Horowitz, D. D. Awschalom, and S. Pennathur, *Lab Chip*, 2008, **8**, 1856-1863.
25. W. Z. Song and D. Psaltis, *Lab Chip*, 2013, **13**, 2708-2713.
26. Y. C. Seow, A. Q. Liu, L. K. Chin, X. C. Li, H. J. Huang, T. H. Cheng and X. Q. Zhou, *Appl. Phys. Lett.*, 2008, **93**, 084101.
27. Y. C. Seow, S. P. Lim and H. P. Lee, *Lab Chip*, 2012, **12**, 3810-3815.
28. Y. Yang, L. K. Chin, J. M. Tsai, D. P. Tsai, N. I. Zheludev and A. Q. Liu, *Lab Chip*, 2012, **12**, 3785-3790.
29. D. B. Wolfe, R. S. Conroy, P. Garstecki, B. T. Mayers, M. A. Fischbach, K. E. Paul, M. Prentiss and G. M. Whitesides, *Proc. Natl. Acad. Sci. U. S. A.*, 2004, **101**, 12434-12438.
30. Y. Yang, A. Q. Liu, L. Lei, L. K. Chin, C. D. Ohl, Q. J. Wang and H. S. Yoon, *Lab Chip*, 2011, **11**, 3182-3187.
31. Y. Yang, A. Q. Liu, L. K. Chin, X. M. Zhang, D. P. Tsai, C. L. Lin, C. Lu, G. P. Wang, and N. I. Zheludev, *Nat. Comm.*, 2012, **3**, 651.
32. T. M. Squires and S. R. Quake, *Rev. Mod. Phys.*, 2005, **77**, 977-1026.
33. A. Safaai-Jazi and V. Suppanitchakij, *IEEE J. Quantum Electron.*, 1997, **33**, 2159-2166.
34. W. J. Tomlinson. *Appl. Opt.*, 1980, **19**, 1127-1138.
35. B. K. Garside, T. K. Lim, and J. P. Marton. *Appl. Opt.*, 1978, **17**, 3670-3674.
36. M. Perumal and K. G. Ranga Raju, *J. Hydrol. Eng.*, 1999, **4**, 160–164.
37. Z. G. Wu and N. T. Nguyen, *Sens. Actuators B*, 2005, **107**, 965–974.
38. K. Okamoto, *Fundamentals of Optical Waveguides*, Academic Press*, San Diego, 2000.
39. L. B. Soldano and E. C. M. Pennings, *J. Lightwave Technol.*, 1995, **13**, 615-627.